Chemical Engineering Journal 415 (2021) 129038

Contents lists available at ScienceDirect

Chemical Engineering Journal

journal homepage: www.elsevier.com/locate/cej

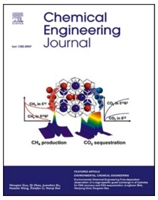

Analyzing industrial CVD reactors using a porous media approach

Siyu Zou[a], Jie Xiao[a,*], Viola Wu[b], Xiao Dong Chen[a,*]

[a] *School of Chemical and Environmental Engineering, College of Chemistry, Chemical Engineering and Materials Science, Soochow University, Suzhou, Jiangsu Province 215123, People's Republic of China*
[b] *INVOTEST BIOTECH CO., LTD, Nantong, Jiangsu Province 226000, People's Republic of China*

ARTICLE INFO

Keywords:
Chemical vapor deposition (CVD)
Numerical simulation
CFD
Porous media
Design and optimization

ABSTRACT

The uniformity of deposited film is a critical quality indicator for the product by chemical vapor deposition (CVD). Quality control of deposited film remains a challenging task, especially for a CVD reactor used in the glass coating process, which often needs to simultaneously process multiple substrate surfaces. So far, an effective method for simulating the multi-substrate CVD reactor used in the glass coating process is unavailable excluding costly direct numerical simulation in real geometry. The numerical simulation and optimization of such a CVD reactor are also lacking. In this paper, a new CFD model was developed to investigate a special industrial-scale multi-substrate CVD reactor for the production of coated glass products. The unique porous media based modeling approach allowed us to efficiently address hundreds or even thousands of spatially-distributed surfaces in one batch of production. Simulation results demonstrate that the mixing performance of the gas reactant in the reactor can be improved by implementing the top-injection scheme, introducing natural convection, and redistributing the substrate surfaces, which can indirectly improve the uniformity of deposited film on the glass. The introduced method is generic and should be an effective tool to understand quality problems in large-scale multi-substrate CVD reactors and hence improve their design and operation.

1. Introduction

Chemical vapor deposition (CVD) is a technology used for solid film formation through chemical reaction of the gas mixture on hot substrate surfaces [1]. It is an advanced and highly promising technology for material purification and preparation [2,3]. In the 19th and 20th centuries, it was first designed to deposit metals (e.g. tungsten, nickel) and silicon [2]. Now, the rapid developments of the microelectronics industry and material science allow CVD technology to be widely used to produce high-performance materials such as polysilicon, graphene, semi-conductors, and Metallo-organic compounds. Such technology can provide better uniformity and controllability of film structures compared with other deposition technologies [2,3]. The CVD reactor is a special reactor, in which interfacial chemical reactions together with momentum, mass, and energy transport takes place simultaneously under high-temperature and low-pressure conditions. Like many other chemical reactors, to achieve the best production efficiency is not an easy task. In order to realize the optimized performance of the CVD process, numerous factors have to be considered, including the morphology and structure of the substrate, pre-treatment method of the precursor gas, the momentum, mass and energy transfer in the gas phase and between substrate surface and gas, and reactor geometry [1]. Thus, it is challenging to design a highly-effective CVD reactor.

A conventional CVD reactor consists of the gas delivery system, the reaction chamber and the exhaust gas treatment system [2,3]. The reaction chamber is the core component. The flow field in the chamber is determined by the geometry (e.g., the inlet and heater locations, the distribution of substrates) and operational conditions of the reactor (e.g., temperature and pressure), which directly influences the uniformity and rate of film growth. According to the difference of the reaction chamber, the industrial CVD reactors can be mainly categorized as three types [1]: the stationary substrate reactor with plug flow [4,5], the pancake rod reactor [6–9], the rotated substrate reactor [10–16]. Each type of reactor can only be applied in limited number of specific industrial processes. A universal CVD reactor suitable for most processes is not available.

Note that the momentum, mass, and energy transfer in the fluid phase, the energy and mass exchange between the fluid and the substrate in the deposition process can all influence deposition rate and uniformity of the film in a complex way. Thus, a systematic and detailed

---

* Corresponding authors.
E-mail addresses: jie.xiao@suda.edu.cn (J. Xiao), xdchen@mail.suda.edu.cn (X.D. Chen).

https://doi.org/10.1016/j.cej.2021.129038
Received 3 June 2020; Received in revised form 4 January 2021; Accepted 15 February 2021

investigation of the CVD process and its influence factors (including operational conditions and structures of the reactor) can provide insights valuable for the improved reactor performance, which will eventually lead to economic and environmental profits.

Although the smoke tracer, laser holography and some in situ experimental techniques [17] can be used to characterize the flow field in a CVD reactor, limited information can be collected [18]. Some physical quantities (e.g., the gas concentration and velocity) can be hardly obtained from experiments. Numerical simulation can provide comprehensive data on the evolution of the flow field and other physical quantities. By resorting to the basic transport theory, the numerical simulation of CVD systems has been extensively conducted.

The CFD has been widely used to design and optimize the structures and operation conditions of CVD reactors. Li et al. [6] introduced proper configurations of gas supplying nozzles and off-gas ports to improve the uniformity of film growth in a Siemens CVD reactor. Li et al. [8] investigated a novel bell-jar reactor with a cooling jacket for each rod, which can provide favorable temperature and velocity profiles by restricting the gas flow between the cooling jacket and rod. Lin et al. [19] introduced an appropriate porous block at the gas inlet to eliminate the recirculation cell caused by a buoyancy effect and also improve the film uniformity. Liao et al. [20] developed a new gas injection system with inlet barriers in CVD reactors to improve the gas distribution. These designs with large or small structural changes effectively improve the performance of CVD reactors. The optimizations of operational conditions have also been conducted. Lubej et al. [4] predicted transport phenomena in the CVD reactor and obtained the optimal substrate temperature. Chuang et al. [5] developed a CFD model coupled with a data-driven optimization scheme to search optimal operating conditions in a set of conditions. Ni et al. [21], Fang et al. [22], Mitrovic et al. [23,24], Tseng et al. [25], Makino et al. [26], and Huang et al. [9] carried out a sensitivity analysis of key factors influencing the growth rate and growth uniformity of the film using numerical simulations. Cho et al. [16] and Gkinis et al. [10] investigated the effect of flow behavior on film uniformity in a rotating-disc CVD reactor. They revealed favorable flow regimes for industrial applications. Li et al. [27] simulated the homogenous reaction, heterogeneous reaction, flow characteristics, and the thermal effect in an impinging CVD reactor. They investigated the effects of reactor-substrate spacing and glass line speed on the deposition profile. Cheimarios et al. [17] and Gakis et al. [15] investigated the flow regime in a rotating disc CVD reactor. The effects of the operation conditions on the flow regime and film growth uniformity were systematically discussed. Nie et al. [28–30] developed a model to investigate thermal behaviors in a Siemens CVD reactor and successfully reduced its energy consumption. These efforts successfully identified improved operation conditions for specific industrial applications.

In this study, the CVD reactor under investigation is a special industrial-scale reactor, which needs to process thousands of coated glass products simultaneously. The existing CVD models that usually deal with one or just a few substrate surfaces cannot be utilized, because explicitly modeling a large amount of substrates in the system geometry is almost computationally impossible. The focus of the current work is to establish a unique modeling method for the simulation of this type of CVD reactor. The idea is to adopt a porous media based method to describe the transport phenomena in the zone with a large number of substrates. Detailed data on the gas flow field, temperature, and concentration distributions can be obtained. The validated model was further used to optimize the design and operation of the reactor.

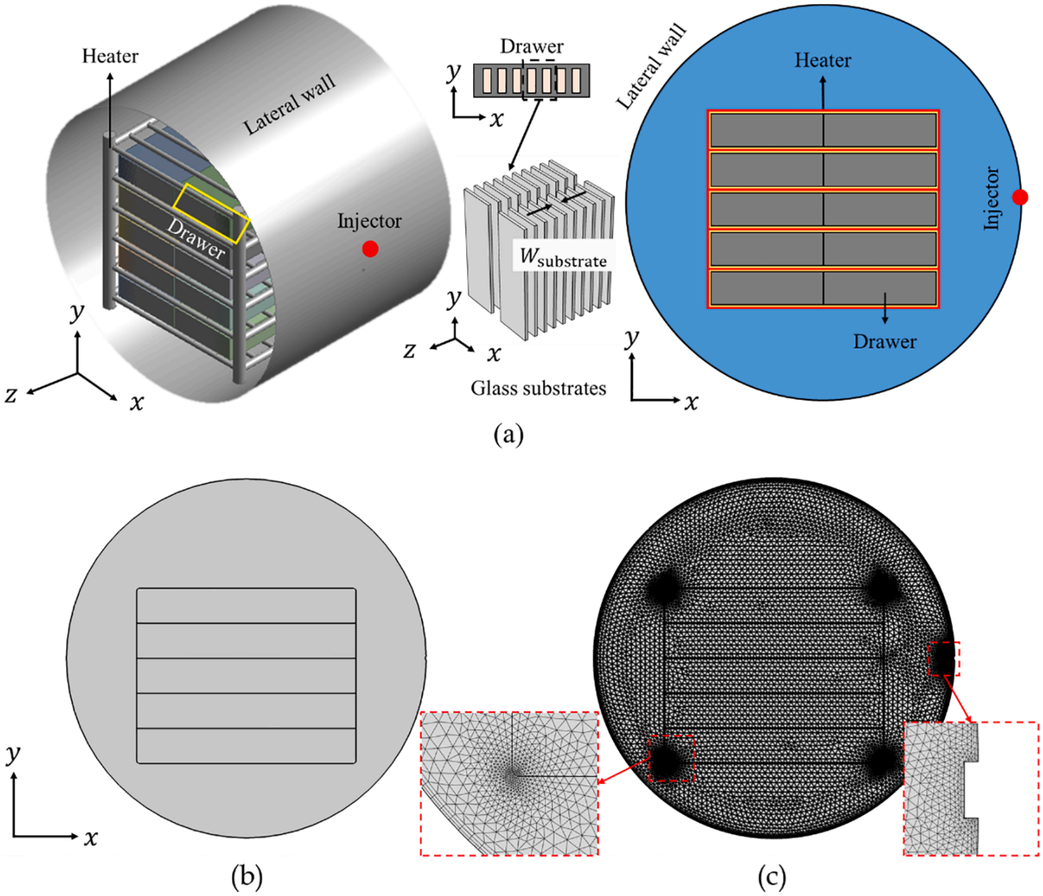

(a)

(b) (c)

Fig. 1. The schematic diagram of the CVD reactor and computational domain showing: (a) the components of the CVD system; (b) a typical computational domain in the base case; (c) the mesh, fine meshes can be found adjacent to the inlet and sharp locations in order to improve the convergence and accuracy of the computation.

2. Modeling and simulation method

Reactor geometry. The CVD reactor simulated in the current work is shown in Fig. 1a, the reaction chamber is a cylinder, the gas delivery system and the exhaust gas treatment system are not shown. The heat exchangers are fixed at the middle section of the reactor. A continuous supply of hot fluid ensures that the heater maintains at a certain temperature. Uncoated substrates are regularly placed in drawers, which are then placed on the heater. The reactant gas is injected from the right side of the reaction chamber, the film will be deposited on the substrate surface after a certain operation time. It should be noted that there are almost twenty thousand substrates in one batch of operation. The drawers packed with thousands of substrates are modeled as porous media. In order to simplify the simulations, a number of assumptions have been made. The porous media are considered isotropic. The isothermal heater is simplified as the line heat source. The gradients of physical quantities along z direction have been neglected, which allows the simulation of a 2D system. Simulations of a 3D reactor have been carried out. It was found that 2D simulation can capture the main flow pattern. The total computational time of a 3D model was almost 8 days. The computational time of a 2D model was, however, only 2 h. Tremendous amount of computational time can be saved (i.e., 96 times difference). The experiments have also been carried out. The measured temperature difference along the z direction was indeed small. Hence, the 2D simplification is reasonable for velocity and temperature prediction. As shown in Fig. 1b, the computational domain is the $x-y$ cross section of the CVD reactor. All dimensions are set according to the actual size of the reactor. Also note that the consumption of reactant is much less than the injected amount. In a real production, the injection amount of reactant in a single batch operation is 0.00452 mol. 20 substrates were sampled to quantify the amount of reactant deposited on the substrate surface. The average deposition amount on each substrate was about 2×10^{-8} mol. The total deposition amount of reactant on all 20000 substrates (in one batch) is around 4×10^{-4} mol, which is about 8.8% of the total injection amount.

Operational procedure. The operation process of this CVD reactor consists of three stages, which are pressure-evacuation, heating-up, and reaction. At first, the air in the reactor chamber is vacuumized and replaced by a small amount of nitrogen, the pressure decreases from 101kPa to almost 5kPa. The heat procedure is then launched to increase the temperature from room temperature to an appropriate reaction temperature, which is almost 90°C in the current CVD reactor. After that, the reactant gas is injected into the reaction chamber. One batch of production is finally completed after reaching a certain reaction time. The pressure evacuation process usually can be controlled well. Hence, the focuses are the heating-up and reaction stages. The simulations have implemented the heating-up and reaction processes to investigate a number of key factors that can influence the CVD process performance. The duration of the heating-up stage is 3600s. After that, the reaction stage lasts 1200s. A 5-sec injection stage is introduced at the beginning of the reaction stage. The total time of a batch operation is 4800s. The reactor is a batch reactor. The following section details the modeling methods used in the current research.

2.1. Governing equations

The flow condition in the CVD reactor needs to be first determined because the flow can possibly transit from viscous flow to molecular flow in a vacuum CVD system [2,3]. The Knudsen number was quantified to estimate whether the continuum hypothesis is applicable. The Knudsen number [31] is defined as,

$$\mathrm{Kn} = \frac{\lambda}{L_{\mathrm{Kn}}} \tag{1}$$

where λ is the mean free path of the gas molecule, m; L_{Kn} is the characteristic length of the system (e.g. $W_{substrate}$ in Fig. 1). In the gas flow, the mean free path of the gas molecule changes with ambient temperature and pressure. Its value can be evaluated based on the kinetic theory [32],

$$\lambda = \frac{k_B T}{\sqrt{2}\pi d^2 p} \tag{2}$$

where k_B is the Boltzmann constant, J/K; T is the ambient temperature, K; d is the molecular diameter, m; p is the ambient pressure, Pa. As the increase of the mean free path of the gas molecule, the probability of intermolecular collisions between molecules becomes lower and the flow can gradually transit to molecular flow. This situation will occur in a CVD reactor which operates at a very high temperature or a very low pressure. In the current system, the Knudsen number varies from $4 \times 10^{-4}\sim 4 \times 10^{-3}$, which is much smaller than the critical value of 0.01. The continuum hypothesis is still valid in this CVD reactor. The Navier-Stokes equations and classical conservation laws of heat and mass have been adopted to simulate the transfer phenomena in this reactor.

The natural convection occurs in the heating-up stage due to non-uniform temperature distribution in the CVD reactor. The Grashof number [33] has been introduced to estimate the flow condition in the CVD reactor, which is defined as,

$$\mathrm{Gr} = \frac{g\beta\Delta T L^3}{\nu} \tag{3}$$

where g is the gravitational acceleration constant, $9.81\mathrm{m/s^2}$; β is the coefficient of thermal expansion, 1/K, it can be treated as 1/T for ideal gases; ΔT is the temperature difference between the heater surface temperature and the bulk gas temperature in the system, K; L is the characteristic length of the system, m, which equals to the height of the porous media in the current reactor; ν is kinematic viscosity defined as the ratio of fluid dynamic viscosity and fluid density, $\nu = \mu/\rho$. In current operational conditions, the Grashof number ranges from 1.79×10^6 to 7.34×10^8, which is less than the critical value of 10^9. Hence, the flow is laminar.

Navier-Stokes equations are used to obtain the momentum profile of the fluid in the CVD reactor. The fluid is treated as a compressible fluid without consideration of work done by pressure changes and viscous dissipation due to the small Mach number in the current system. Meanwhile, the governing equations of the free flow area and the porous flow area are different. They are listed in the following text respectively (also see Fig. 2).

The vector form of the momentum conservation equations for the free flow area (also see Fig. 2) can be written as,

$$\frac{\partial \rho_f}{\partial t} + \nabla\cdot(\rho_f \boldsymbol{u}) = 0 \tag{4}$$

$$\rho_f \frac{\partial \boldsymbol{u}}{\partial t} + \rho_f \boldsymbol{u}\cdot\nabla\boldsymbol{u} = -\nabla p + \nabla\cdot\left(\mu\left(\nabla\boldsymbol{u} + (\nabla\boldsymbol{u})^T\right) - \frac{2}{3}\mu(\nabla\cdot\boldsymbol{u})\boldsymbol{I}\right) + F_g \tag{5}$$

where ρ_f is the fluid density, $\mathrm{kg/m^3}$; $\boldsymbol{u}$ is the velocity vector, m/s; t is time, s; p is pressure, Pa; μ is the fluid dynamic viscosity, Pa·s; F_g is the gravitational body force, $\mathrm{N/m^3}$.

The vector form of the momentum conservation equations of the porous flow area (also see Fig. 2) [34-36] can be written as,

$$\varepsilon\frac{\partial \rho_f}{\partial t} + \nabla\cdot(\rho_f \boldsymbol{u}) = 0 \tag{6}$$

$$\frac{\rho_f}{\varepsilon}\left(\frac{\partial \boldsymbol{u}}{\partial t} + (\boldsymbol{u}\cdot\nabla)\frac{\boldsymbol{u}}{\varepsilon}\right) = -\nabla p + \nabla\cdot\frac{1}{\varepsilon}\left(\mu\left(\nabla\boldsymbol{u} + (\nabla\boldsymbol{u})^T\right) - \frac{2}{3}\mu(\nabla\cdot\boldsymbol{u})\boldsymbol{I}\right) - \frac{\kappa}{\mu}\boldsymbol{u} + F_g \tag{7}$$

where ε is the porosity of the porous medium, 1; κ is the permeability of

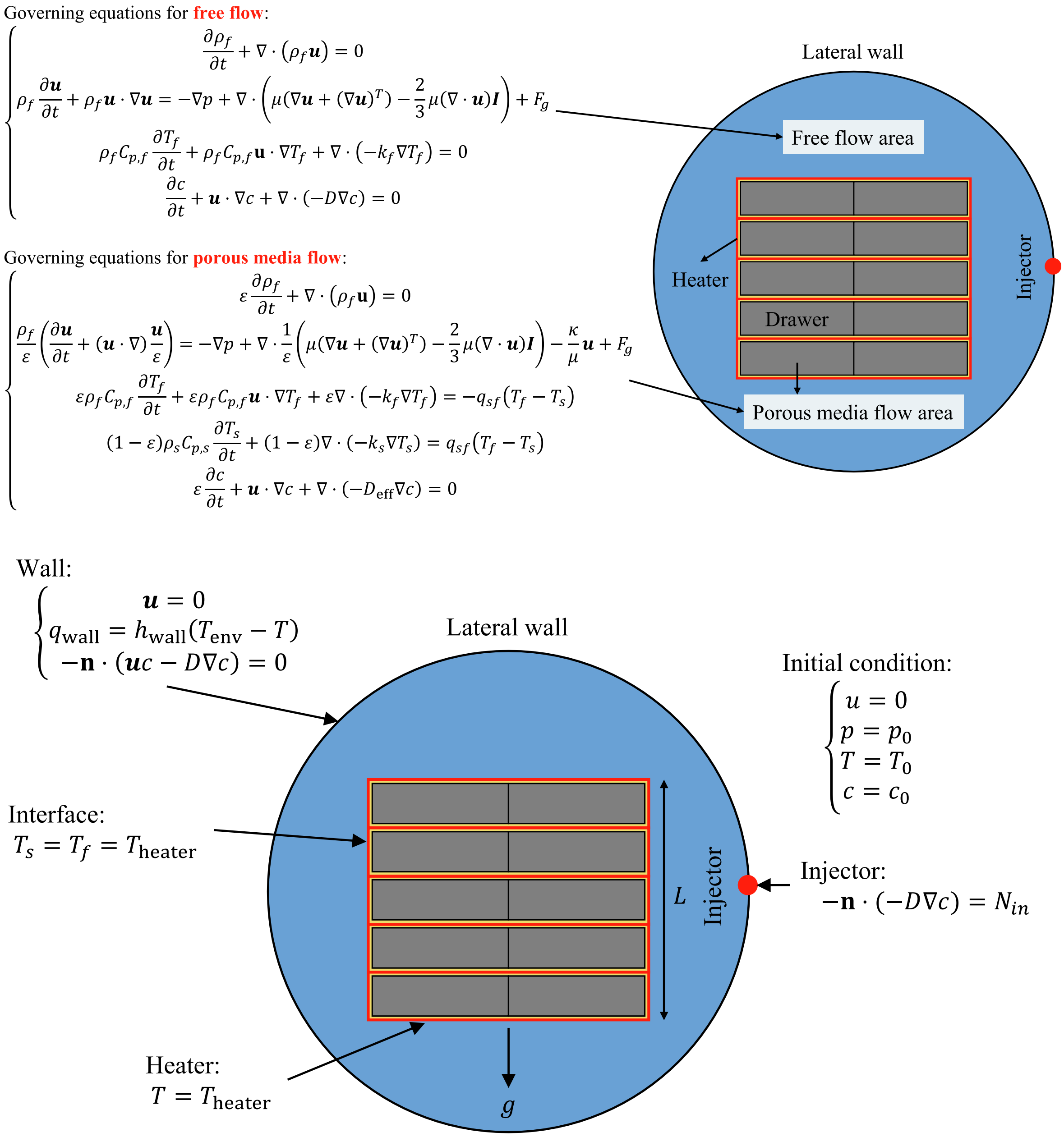

Fig. 2. Illustration of the governing equation, the initial conditions, and the boundary conditions.

the porous medium, m^2. In current simulations, the porous media is a kind of pin–fin structure. Hence, the porosity was determined by the geometry of the system. The permeability was calculated by the empirical correlation obtained from the literature [37,38]. The fourth term on the right-hand side of equation (7) represents the resistance encountered by the fluid flowing through the porous medium.

The fluid density and dynamic viscosity are dependent on fluid temperature. It is assumed to obey the ideal gas law,

$$\rho_f = \frac{pM_f}{RT_f} \tag{8}$$

where M_f is the molecular mass of the fluid, kg/mol; R is the ideal gas constant, J/(mol·K); p is fluid pressure, Pa; T_f is fluid temperature, K.

The temperature is obtained by solving energy conservation equations. In the free flow area, energy conservation is described by the convection–diffusion equation (also see Fig. 2). Its vector form can be written as,

$$\rho_f C_{p,f} \frac{\partial T_f}{\partial t} + \rho_f C_{p,f} \boldsymbol{u} \cdot \nabla T_f + \nabla \cdot \left(-k_f \nabla T_f\right) = 0 \tag{9}$$

where $C_{p,f}$ is the specific heat capacity of the fluid, J/(kg·K); k_f is the thermal conductivity of the fluid, W/(m·K).

The energy conservation equations of the porous flow area are also different from those of the free flow area. The porous medium consists of fluid and solid matrix. The local thermal equilibrium hypothesis can be adopted if the energy transfer efficiency is high enough, which means the fluid and the solid have the same temperature. In our cases, the difference between the heat capacities of the fluid and solid is modest. But the density difference is huge. It means the temperature increase of solid is much slower than fluid when the energy supply is equal. Throughout the complete operation, the solid temperature was always lower than the fluid temperature. Our experiments also confirmed this phenomenon. Hence, the local thermal equilibrium hypothesis cannot be used, and the temperature distribution in the porous medium has to be considered.

The local thermal non-equilibrium method [34] has been applied in the porous flow area (also see Fig. 2). It solved two coupled energy equations. The convection–diffusion equation is used to describe the heat transfer in the fluid area of the porous medium. The heat transfer in the solid area of the porous medium is solved by the pure diffusion equation. The additional source terms at the right end of the energy Eqs. (10) and (11) are used to quantify heat exchange between two phases.

$$\varepsilon\rho_f C_{p,f}\frac{\partial T_f}{\partial t}+\varepsilon\rho_f C_{p,f}\boldsymbol{u}\cdot\nabla T_f+\varepsilon\nabla\cdot\left(-k_f\nabla T_f\right)=-q_{sf}\left(T_f-T_s\right) \tag{10}$$

$$(1-\varepsilon)\rho_s C_{p,s}\frac{\partial T_s}{\partial t}+(1-\varepsilon)\nabla\cdot\left(-k_s\nabla T_s\right)=q_{sf}\left(T_f-T_s\right) \tag{11}$$

where ρ_s is the solid density, $\mathrm{kg/m^3}$; $C_{p,s}$ is the specific heat capacity of the solid, $\mathrm{J/(kg\cdot K)}$; T_s is solid temperature, K; k_s is the thermal conductivity of the solid, $\mathrm{W/(m\cdot K)}$; q_{sf} is the interstitial convective heat transfer coefficient, $\mathrm{W/(m^3\cdot K)}$, which is defined as,

$$q_{sf}=a_{sf}h_{sf} \tag{12}$$

where a_{sf} is the specific surface area between solid and fluid in the porous medium, $\mathrm{m^2/m^3}$. It can be evaluated based on the porosity due to the simple structure of the porous medium in the current case. h_{sf} is the interstitial heat transfer coefficient between fluid and substrate wall, $\mathrm{W/(m^2\cdot K)}$. It is calculated by the Nusselt number derived from the plate heat transfer correlation [39],

$$\mathrm{Nu}=\frac{h_{sf}L}{k_f}=0.664\mathrm{Re}^{1/2}\mathrm{Pr}^{1/3} \tag{13}$$

where Nu is the Nusselt number; Re is the Reynolds number, 1; Pr is the Prandtl number; L is the characteristic length of the system, m, which equals to the height of the porous media zone in the current reactor (see Fig. 2).

The reactant is treated as a dilute species due to the small amount of the reactant in the CVD reactor. The properties of the carrier gas (the nitrogen in the current reactor) such as density, viscosity are not affected by the reactant. Hence, the mass conservation and energy conservation are similar, all subjected to the convection–diffusion equation in the fluid system. The vector form of the mass conservation equations (also see Fig. 2) for the free flow area can be written as,

$$\frac{\partial c}{\partial t}+\boldsymbol{u}\cdot\nabla c+\nabla\cdot(-D\nabla c)=0 \tag{14}$$

where c is the reactant concentration in the fluid, $\mathrm{mol/m^3}$; D is the reactant diffusion coefficient in nitrogen at the free flow area, $\mathrm{m^2/s}$. It can be evaluated by the Fuller correlation [32],

$$D_{AB}=\frac{0.00143T^{1.75}}{p_{\mathrm{bar}}M_{AB}^{1/2}\left(V_A^{1/3}+V_B^{1/3}\right)^2} \tag{15}$$

where D_{AB} is the binary diffusion coefficient, $\mathrm{cm^2/s}$; T is the temperature, K; M_A and M_B are molecular weights of species A and B, $\mathrm{g/mol}$; p_{bar} is the system pressure, bar; V_A and V_B are the sums of atomic diffusion volumes of each component, whose values can be found in the literature [40,41]. The unit conversion needs to be performed in this empirical correlation. The diffusion coefficient of the gas reactant is related to gas temperature and pressure, for example, at 90°C and 5kPa, $D = 1.584\times 10^{-4}\mathrm{m^2/s}$.

The vector form of the mass conservation equations for the porous flow area (also see Fig. 2) can be written as,

$$\varepsilon\frac{\partial c}{\partial t}+\boldsymbol{u}\cdot\nabla c+\nabla\cdot\left(-D_{\mathrm{eff}}\nabla c\right)=0 \tag{16}$$

where D_{eff} is the effective diffusion coefficient in the porous flow area, $\mathrm{m^2/s}$. It can be evaluated from the model provided by Millington and Quirk [42],

$$D_{\mathrm{eff}}=\varepsilon^{4/3}D \tag{17}$$

where D is the binary diffusion coefficient in the free flow area, $\mathrm{m^2/s}$. It should be noted that the reaction source term hasn't been considered in the current simulation due to the small amount of mass consumed by the reaction as compared to the amount from injection.

The material properties of the fluid in the CVD reactor chamber are assumed equal to the material properties of pure nitrogen. The values are evaluated based on the following polynomial equation related to temperature [43],

$$\mu=1.77230303\times10^{-6}+6.27427545\times10^{-8}T_f-3.47278555\times10^{-11}T_f^2+1.01243201^{-14}T_f^3 \tag{18}$$

$$C_{p,f}=1088.22121-0.365941919T+7.88715035\times10^{-4}T_f^2-3.749223\times10^{-7}T_f^3+3.17599068\times10^{-11}T_f^4 \tag{19}$$

$$k_f=3.6969697\times10^{-4}+9.74353924\times10^{-5}T_f-4.07587413\times10^{-8}T_f^2+7.68453768\times10^{-12}T_f^3 \tag{20}$$

Compared to gas, the material properties of solid are insensitive to the change of temperature [32]. Hence, the material properties of solid are treated as constants. The solid in the porous medium is SiO_2 (vitreous), the corresponding material properties used in current simulations are listed in Table 1.

2.2. Initial and boundary conditions

The nitrogen with a constant temperature T_0 and pressure p_0 is filled into the reaction chamber. The initial concentration of gas reactant is $c_0 = 0\mathrm{mol/m^3}$. The gravitational volume force has been applied in the whole fluid domain. The heating temperature is set to T_{heater}. At lateral walls of the reactor chamber, the no-slip boundary conditions and the no flux boundary condition are respectively specified for the momentum transfer equation and the mass transfer equation. The convective heat flux is set as a boundary condition for energy equations on the lateral walls. It interprets the convective heat loss at the reactor surface in current simulations.

$$q_{\mathrm{wall}}=h_{\mathrm{wall}}\left(T_{\mathrm{env}}-T_f\right) \tag{21}$$

where q_{wall} is the convection heat flux of the lateral walls, $\mathrm{W/m^2}$; h_{wall} is the heat transfer coefficient between the external fluid and the CVD reactor wall, $\mathrm{W/(m^2\cdot K)}$; T_{env} is the environmental temperature, K, which is assumed as a constant of 298K in current simulations.

The injection process before the start of the reaction stage has been simulated as the boundary condition of inlet flux. The value of N_{in} is calculated based on the molar amount of the injected reactant, the inlet area of the injector and the injection time,

$$-\mathbf{n}\cdot(-D\nabla c)=N_{\mathrm{in}}=\frac{n_{\mathrm{inject}}}{t_{\mathrm{inject}}s_{\mathrm{inject}}} \tag{22}$$

where n_{inject} is the molar amount of the injected reactant, mol; t_{inject} is the

Table 1
The material properties of SiO_2 (vitreous).

Material properties	Value
Density (ρ_s)	$2196\mathrm{kg/m^3}$
Heat capacity ($C_{p,s}$)	$823.4\mathrm{J/(kg\cdot K)}$
Thermal conductivity (k_s)	$1.4\mathrm{W/(m\cdot K)}$

injection time, s; s_{inject} is the inlet area of the injector, m^2.

The heater is simplified as isothermal line heat source, which is also the interface between the porous flow area and free flow area.

$$T_s = T_f = T_{\text{heater}} \tag{23}$$

All boundary conditions and initial conditions are summarized in Table 2 and Fig. 2.

2.3. *Numerical implementation*

In this work, all PDEs were solved using COMSOL Multiphysics [44] software. These numerical procedures were realized using the finite-element method and iterated to a residual of less than 0.001 to obtain a converged solution. The numerical scheme of the time-dependent problem is Backwards differentiation formula (BDF) method. The tolerance mentioned in the current study is relative tolerance. The basis function of pressure (p), velocity (u, v), fluid temperature (T_f) and concentration (c) is Linear Lagrange function. For solid temperature (T_s), it's Quadratic Lagrange function. After solving the coupled equations, the detailed spatial and temporal distributions of fluid velocity, reactant concentration, the temperature of solid and fluid and other information can be obtained and analyzed.

The free triangular meshes are applied for the whole computational domain except for the boundary layer area. Three layers of the boundary layer mesh are generated to capture the sharp gradient near the lateral wall of the reaction chamber. The extra mesh refinements are adopted at some sharp contact points between the free flow area and the porous flow area in order to facilitate computational convergence. Similarly, the finer mesh was generated at the inlet boundary to accurately calculate the inlet amount. A typical mesh is shown in Fig. 1c.

2.4. *Model validations*

The numerical model is verified against two sets of experimental data of temperature obtained in the CVD reactor. Two sampling locations of temperature are depicted in Fig. 3. Note that there are two thermocouples in each location. One thermocouple is placed on the substrate and the other is used to measure the temperature of gas adjacent to the substrate. The sampling interval was 1s. In the validation experiments, the reaction chamber was vacuumed and then injected with pure nitrogen. Note that the operation conditions of the validation experiments are different from those in the production process. The operational pressure of the validation experiment is almost equal to one atm. The heater temperature is 95 °C. The heating-up procedure was launched after the system was stabilized for 4120s. The operational conditions of the validation experiment and simulation are listed in Table 3.

The temperature evolutions are shown in Fig. 3. The same trend can be observed. It can be found that a larger deviation can be observed at sampling location 1. The deviation in the early stage is larger than that in the later stage, and the deviation in the later stage falls within ±5%. During the whole process, the largest deviation is less than ±15%. Hence, it can be concluded that the prediction accuracy of the numerical model is acceptable.

Table 2
The initial, boundary conditions and other parameters of the base case.

Variables	Values
Initial velocity,u_0	0m/s
Initial pressure,p_0	5kPa
Initial temperature of the gas,$T_{f,0}$	30°C
Initial temperature of substrates,$T_{s,0}$	30°C
Initial concentration of reactant,c_0	0mol/m^3
Heater temperature,T_{heater}	90°C
Wall heat transfer coefficient,h_{wall}	$\approx 0\text{W/(m}^2\cdot\text{K)}$
Inlet flux,N_{in}	$\approx 0.09\text{mol/(m}^2\cdot\text{s)}$
Porosity of porous media,ε	$\approx 1/3$
Specific area of porous media,a_{sf}	$\approx 368\text{m}^2/\text{m}^3$
The gap in porous media	0m
Injector position	Right

3. Results and discussion

In this section, the base case is analyzed first, whose settings represent a real production in the factory. Then, the effects of the reactor structure and operational conditions on gas distribution uniformity are investigated to pursue the improvement strategy.

3.1. *Base case analysis*

Four different meshes have been designed for a mesh independence study. As shown in Fig. 4, the temperature only demonstrates relatively small differences as the number of elements increases. It is demonstrated that the numerical simulation is insensitive to the mesh changes in the current range. Consider the computational time and cost, the configurations of mesh 3 are applied in the following simulations.

The initial, boundary conditions and other parameters of the base case are listed in Table 2 and Table 4. The evolution of the velocity distribution of the base case is illustrated in Fig. 5a. Note that the data range of velocity are adjusted to be the same for all time instants in order to facilitate comparison. Note that the vector arrows of velocity are only plotted to visualize the flow direction. At the initial heating-up stage, the natural convection can be observed (see the plot at 120 s). However, the intensity of the convection decreases gradually as the time proceeds. Convection can be hardly observed at 3600 s, which is the beginning of the reaction stage, implying that the gas reactant injected into the reactor can't be transferred by convection efficiently.

Fig. 6a illustrates the evolution of the average fluid velocity of the whole reactor, in which Case 1 is the base case. It can be found that the velocity generated by natural convection decreased dramatically in the first 300 s (heating-up stage). After that, the velocity decreased further and maintained at low values. Gas reactant could not be effectively distributed in the reaction stage by convective transport. Fig. 6b depicts the evolution of the average fluid velocity in the porous media (i.e., the zone with substrate surfaces to be processed). The velocity in the porous media decreased steadily during the whole process, which is caused by the decrease of the temperature difference between the fluid and the substrate surface as a function of time. The above analyses show that the natural convection was almost negligible in the base case, which will result in the poor distribution uniformity of gas reactant and hence poor uniformity of film growth in the CVD reactor.

The evolution of the concentration distribution of the gas reactant is plotted in Fig. 7a. The semicircular concentration profiles indicate the mass transport is diffusion dominated. The characteristic time of molecular diffusion was introduced to quantify the role of diffusion. It is defined as $t_D = L_D^2/D$, where L_D is characteristic length of diffusion (i.e., reactor diameter in the current simulation, m), D is the molecular diffusivity m^2/s). Under current operational conditions, the characteristic time of molecular diffusion is about 2.8 h, which is much larger than the total time of the reaction stage (i.e. 1200 s). It means that the mixing level of the gas reactant can't approach a decent state even at the end of the reaction stage.

In order to quantify the mixing performance of the gas reactant in the CVD reactor, the mixing level proposed in [45,46] was adopted in current simulations.

The mixing level of each element at time t can be defined as,

$$\chi_{i,t} = \begin{cases} \dfrac{c_{i,t}}{c_\infty}, if(c_i \le c_\infty) \\ \dfrac{c_0 - c_{i,t}}{c_0 - c_\infty}, if(c_i > c_\infty) \end{cases} \tag{24}$$

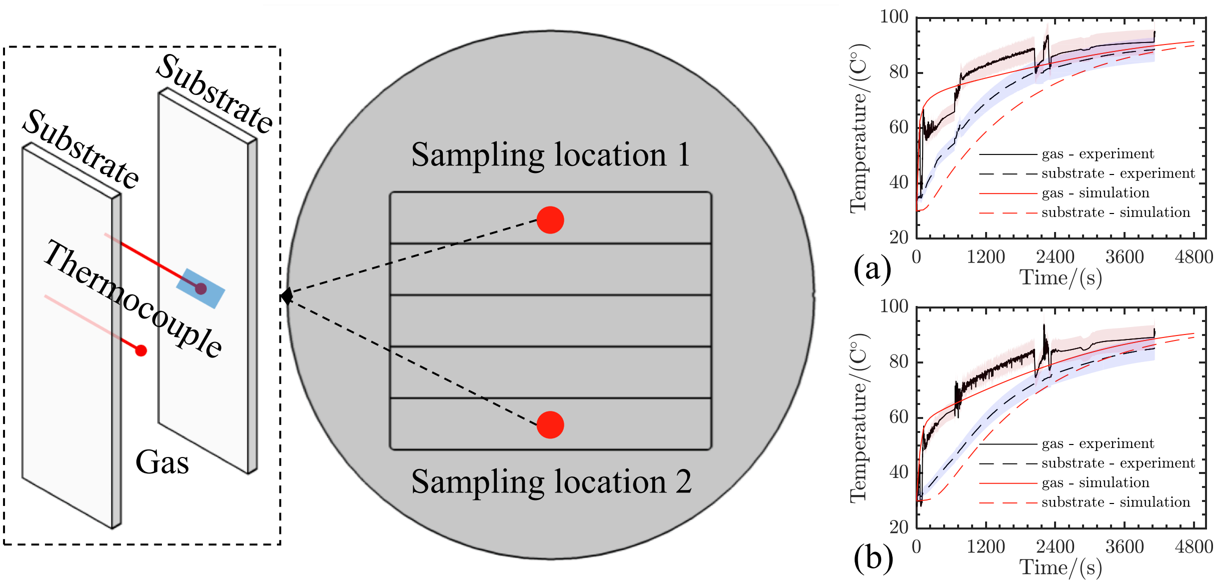

Fig. 3. The temperature evolution at two sampling locations (comparison between experimental data and model predictions): (a) the evolution of gas and substrate temperature at sampling location 1, (b) the evolution of gas and substrate temperature at sampling location 2.

Table 3
The initial and boundary conditions of the validation case.

Variables	Value
Initial velocity,u_0	$0\mathrm{m/s}$
Initial pressure,p_0	$101\mathrm{kPa}$
Initial temperature of the gas,$T_{f,0}$	$30^{\circ}\mathrm{C}$
Initial temperature of substrates,$T_{s,0}$	$30^{\circ}\mathrm{C}$
Heater temperature,T_{heater}	$95^{\circ}\mathrm{C}$
Heat transfer coefficient of the wall,h_{wall}	$\approx 0\mathrm{W/(m^2{\cdot}K)}$
Porosity of porous media,ε	$\approx 1/3$
Specific area of porous media,a_{sf}	$\approx 368\mathrm{m^2/m^3}$
The gap in porous media	$0\mathrm{m}$

where, $\chi_{i,t}$is local mixing level in element i at time t; $c_{i,t}$is local concentration in element i at time t, $\mathrm{mol/m^3}$; c_∞ is the average concentration in a well-mixed system, $\mathrm{mol/m^3}$; $c_0$is the initial concentration in the system, $\mathrm{mol/m^3}$.

The overall mixing level at time t for the whole system can be calculated as,

$$\chi_t = \frac{\sum_{i=1}^{n} (\chi_{i,t} \cdot V_{i,mesh})}{\sum_{i=1}^{n} V_{i,mesh}} \tag{25}$$

where χ_t is mixing level at time t; $V_{i,mesh}$is the volume of element i, $\mathrm{m^3}$.

More details about the calculation method of mixing level can be found in those two papers. The time when mixing level reaches $99 \pm 0.5\%$ is defined as the mixing time. Moreover, the total time of the reaction stage is set as the mixing time if the mixing level can't reach the defined criterion at the end of the reaction stage. As shown in Fig. 8a, a mixing level approaching 100% indicates a thorough mixing. Fig. 8a shows the evolution of the mixing level in the porous media zone. The maximum mixing levels are about 74.21% for the base case, which means that the gas reactant can't reach perfect mixing during the reaction stage and thus uniform film can't be obtained on the substrate surfaces. Fig. 8b shows the mixing time. It is equal to the duration of the reaction stage, also indicating the poor mixing performance in the base case. These findings are consistent with conclusions drawn from velocity field analyses.

3.2. Enhanced convection by substrate distribution design

A most effective method for the improvement of mixing performance is to introduce convection. In the current work, a gap can be introduced in the middle of the porous media due to the symmetry of the reactor to improve the permeability of the porous media. It can be realized by changing the distribution of substrates in the reactor. A big drawer can be replaced by two small drawers placed side by side with a gap in between. The detailed settings are listed in Table 4 (see Case 2). Fig. 5b illustrates the evolution of the velocity field. It can be observed that a high-velocity flow was generated inside the gap. Based on the direction of the velocity vector, such convection can efficiently transport the gas reactant from the top to the bottom of the reactor. Although the convection intensity decayed over time, the velocity was still much larger than the base case (also see Fig. 6). As shown in Fig. 6a, the average velocity in the whole reactor decreased continuously after 300 s. It was about $0.0037\mathrm{m/s}$ at the beginning of the reaction stage (i.e. 3600 s), which can contribute to the distribution of the gas reactant. Fig. 7b demonstrates the evolution of the concentration distribution for Case 2. The mixing of gas reactants reached a relatively uniform level in the middle of the reaction stage (i.e. 4200 s). A well-mixed state was achieved at 4800 s. Fig. 8a shows the evolution of the mixing level. The final mixing level can reach 100% in the porous media zone. Fig. 8b shows that the mixing time of Case 2 is about 780 s. The drastic reduction of mixing time as compared with the base case indicates a much faster mixing of the gas reactant, hence the improvement of the thickness uniformity of the deposited film. It can be concluded that decent convection is critical for the mixing of the gas reactant.

3.3. Enhanced convection by wall insulation design

Generating convection by manipulating boundary conditions (such as the heat loss from the reactor) is another feasible approach for an enhanced convection. Different from the reactor in Case 1 having ideal heat insulation, heat loss was introduced for the reactor in Case 3 (see the settings in Table 4). The natural convection was generated and maintained over the whole operation process (Fig. 5c). There was almost no decay of the convection intensity. The quantitative analysis of average velocity is depicted in Fig. 6. The average velocity in the whole reactor remained stable after 300s. This is mainly due to the continuous natural convection caused by stable heat loss to the environment. As

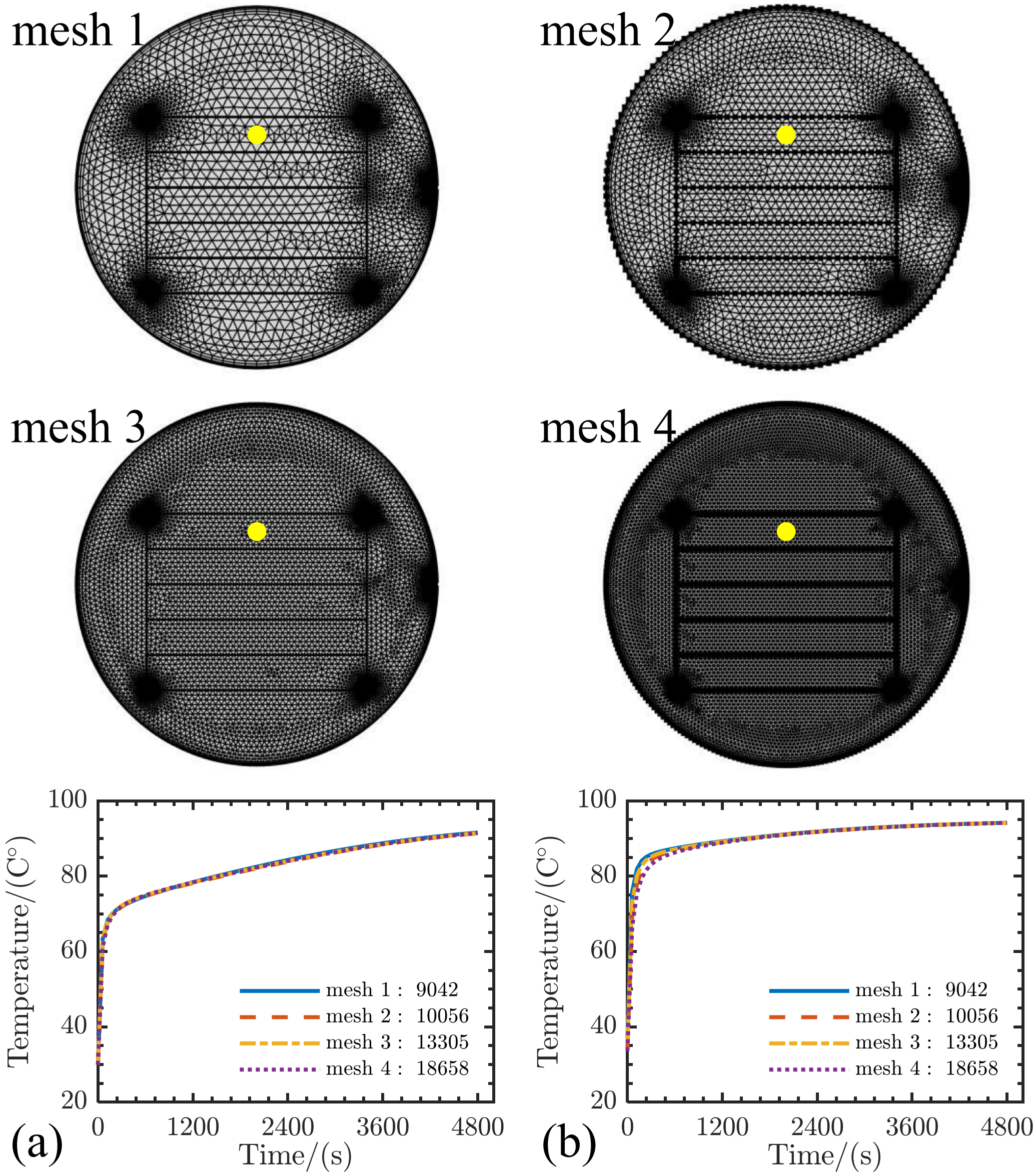

Fig. 4. Comparison of results under the mesh with different number of elements: (a) the fluid temperature evolution at the sampling point depicted in yellow; (b) the evolution of the average fluid temperature of the whole reactor.

Table 4

The parameters and boundary conditions for different cases, the other parameters are the same as the base case (see Table 2).

Case type	The gap width in porous media	Heat transfer coefficient of wall	Injector position
Case 1 (base case)	0m	$0\mathrm{W}/(\mathrm{m}^2\cdot\mathrm{K})$	Right
Case 2	0.05m	$0\mathrm{W}/(\mathrm{m}^2\cdot\mathrm{K})$	Right
Case 3	0m	$0.01\mathrm{W}/(\mathrm{m}^2\cdot\mathrm{K})$	Right
Case 4	0m	$0\mathrm{W}/(\mathrm{m}^2\cdot\mathrm{K})$	Top
Case 5	0.05m	$0\mathrm{W}/(\mathrm{m}^2\cdot\mathrm{K})$	Top
Case 6	0m	$0.01\mathrm{W}/(\mathrm{m}^2\cdot\mathrm{K})$	Top

shown in Fig. 9, the wall temperature reached the temperature of the heater (i.e. 90°C) in Case 1 and Case 2 within 300 s, indicating the disappearance of temperature differences in a short period of time. Thus the natural convection in Case 1 and Case 2 decayed quickly. For three cases, the lowest average wall temperature and average fluid temperature can be observed for Case 3. It means that Case 3 demonstrated the maximal temperature difference between the heater and the reactor wall, which offered the driving force for natural convection generation. Fig. 7c indicates that the reactant gas was distributed rapidly by such convection and filled the right half of the reactor within 60s. A well-mixed state could be reached at 4800s. A shorter mixing time can be observed for Case 3 compared to Case 1 (Fig. 8).

3.4. Improved performance by injection scheme design

Based on the analyses of the flow fields in Case1, Case2, Case3, it can be found that the natural convection was originated from the region near the heater (see the vector arrows of velocity in Fig. 5a–c), where the maximal temperature difference exists at initial time. The fluid first rose up from the region near the heater to the top of the reactor and then flowed downwards after touching the top of the reactor wall. It can be found that the flow field is symmetric in all cases and a key feature is that a downward convection can be observed in the reactor regardless of the direction of the vortex. In Case 1 and Case 2 (see Fig. 5a, b), the

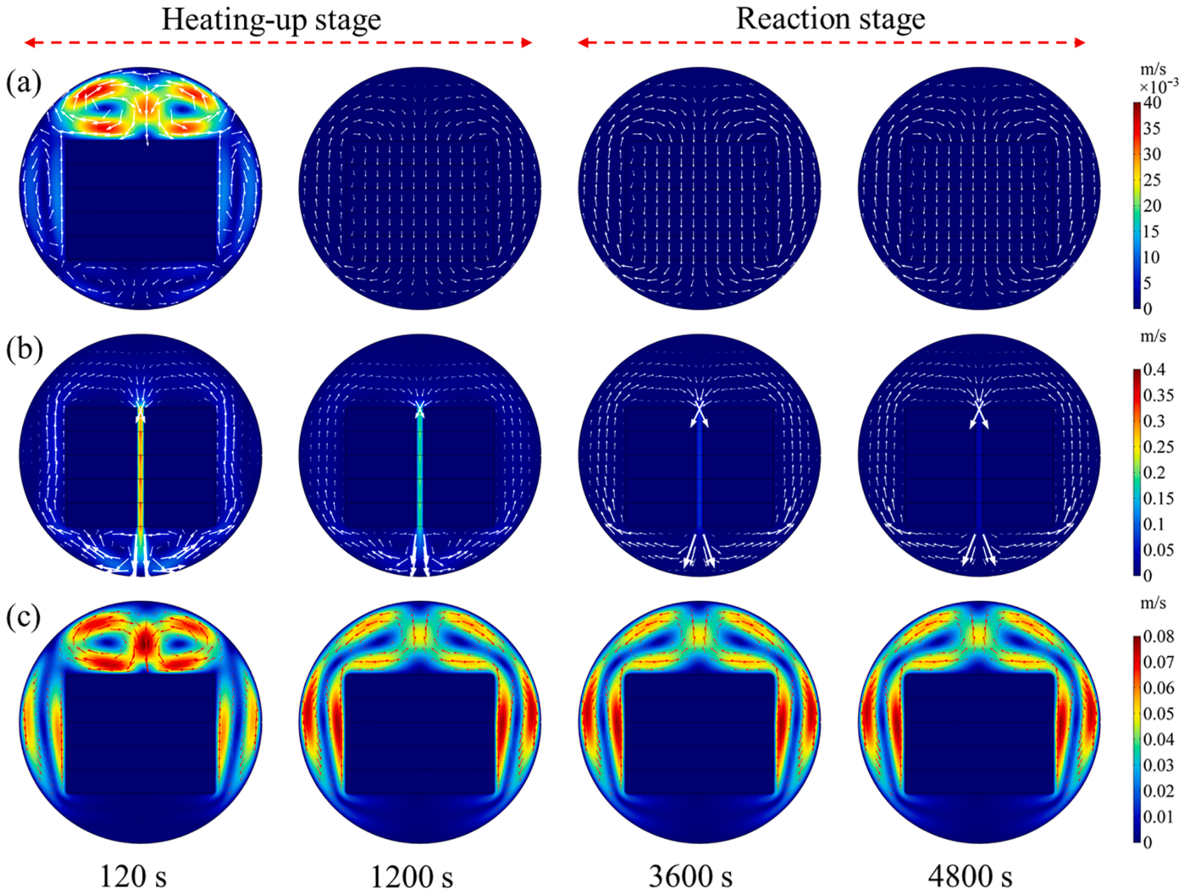

Fig. 5. The evolution of velocity distribution in the CVD reactor: (a) is the base case (i.e. Case 1); (b) is the case containing a gap in the porous media (i.e. Case 2); (c) is the case with heat loss, $h_{\text{wall}} = 0.01\text{W}/(\text{m}^2{\cdot}\text{K})$ (i.e. Case 3).

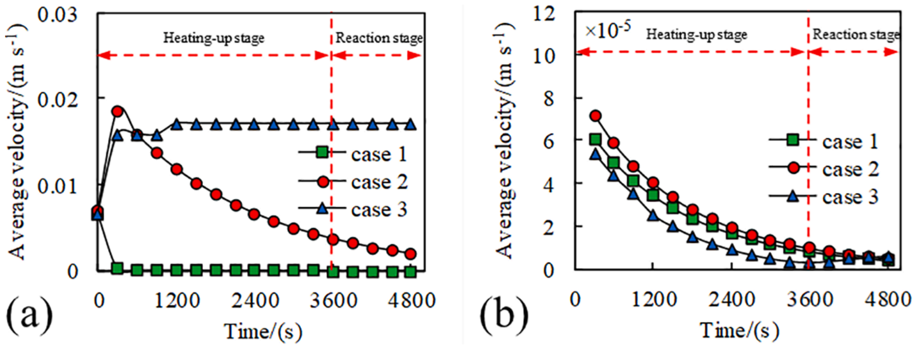

Fig. 6. The evolution of the average fluid velocity in the CVD reactor: (a) is the average fluid velocity of the whole reactor; (b) is the average fluid velocity in the porous media.

downward convection with maximal intensity is observed in the middle of the reactor. In Case 3 (see Fig. 5c), the downward convection with maximal intensity can be observed near the reactor wall. Moving the injector to the top of the reactor can effectively utilize this flow pattern and the convection with the maximal intensity, hence the gas reactant can be distributed symmetrically and rapidly to the reaction chamber along the streamlines. Therefore, Case 4, Case 5 and Case 6 were designed to investigate the effect of injection scheme on the gas distribution. The injectors for three cases are all placed at the top of the reactor, all the other conditions are the same as those in Case 1, Case 2 and Case 3 respectively.

The flow fields of these cases are identical to those in Case 1, Case 2 and Case 3 respectively. Fig. 10 demonstrates the evolution of the concentration distribution. As for Case 4, the dominant mechanism of mass transport is molecular diffusion. Significant concentration gradients can be observed even at the end of the process (see Fig. 10a). The mixing states for Case 5 and Case 6 were totally different (see Fig. 10b, c). Symmetrical concentration distribution patterns can be observed and the gas reactant were well mixed at 4800s.

The evolutions of mixing level and mixing time are plotted in Fig. 11 for further analysis. The mixing level of Case 5 and Case 6 increased to a slightly higher value in a shorter time when compared to Case 2 and Case 3, respectively. But Case 4 demonstrated slightly worse mixing level in the porous media zone as compared with that in Case 1, that mainly attributes to the longer distance between the porous media and the injector in Case 4. The mixing time data illustrated in Fig. 11b

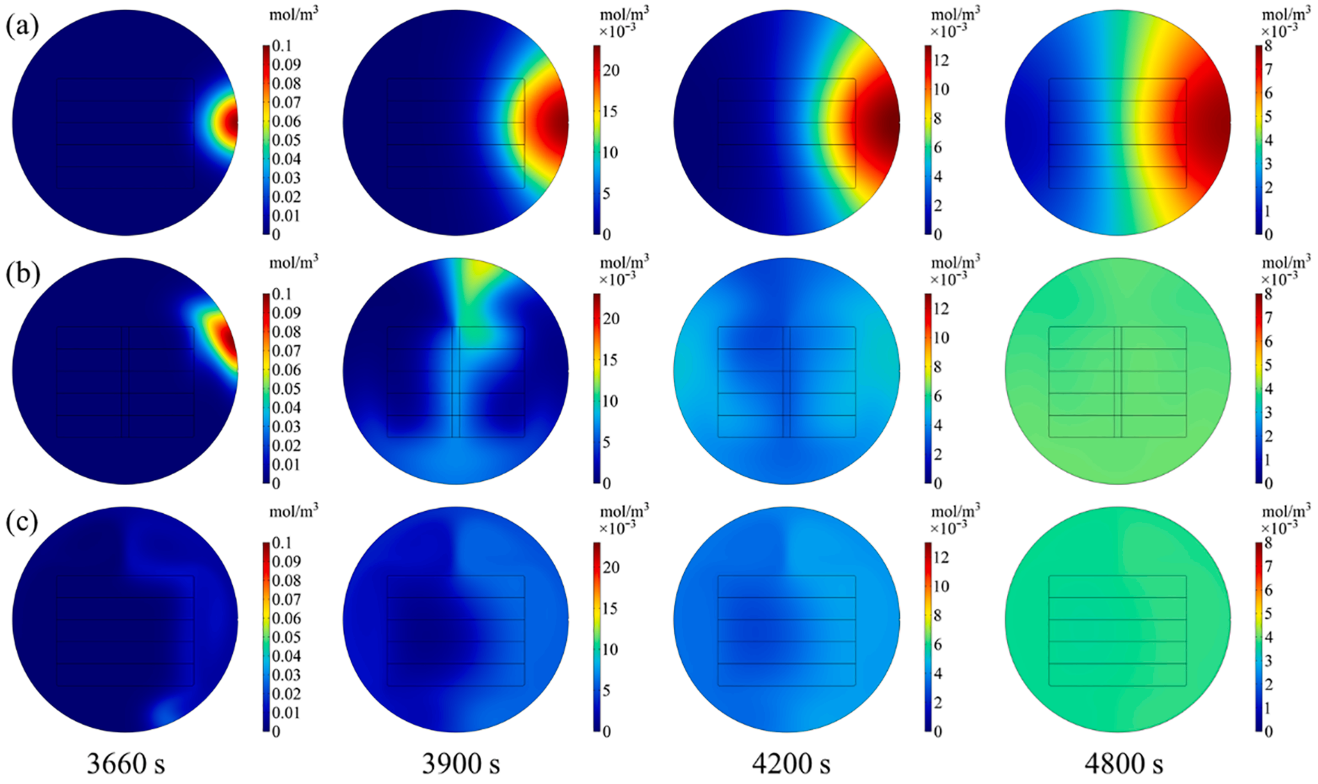

Fig. 7. The evolutions of the concentration distribution of the gas reactant in the CVD reactor: (a) Case 1 (base case); (b) Case 2; (c) Case 3.

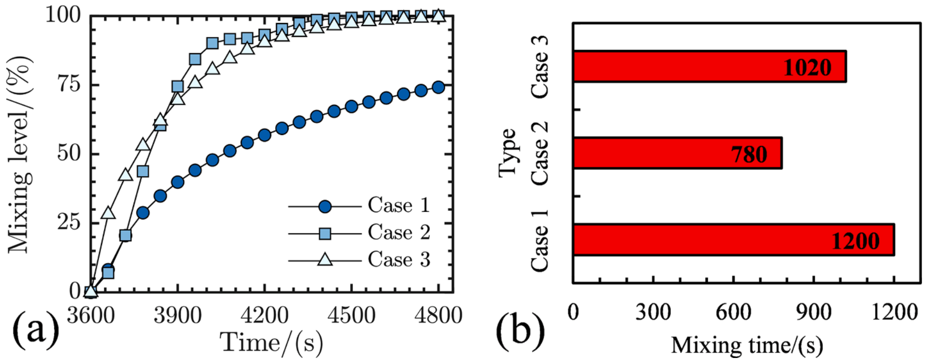

Fig. 8. Comparison of the mixing level and the mixing time between cases: (a) the evolution of the mixing level in the porous media zone; (b) the mixing time in the porous media zone.

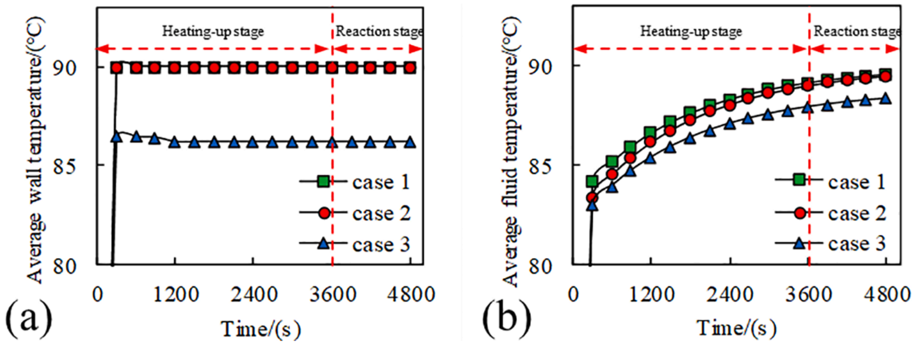

Fig. 9. The evolution of the average temperature in the CVD reactor: (a) is the average wall temperature; (b) is the average fluid temperature.

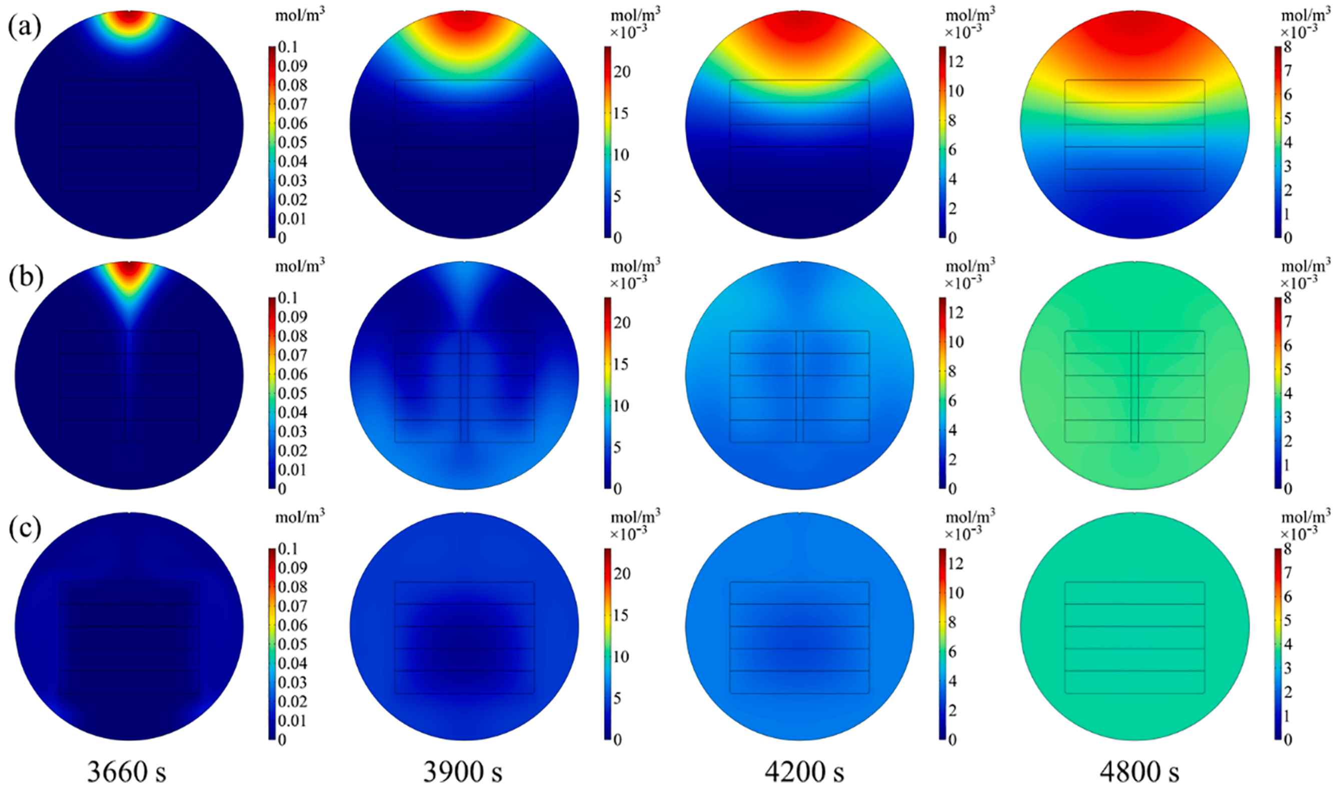

Fig. 10. The evolution of the concentration distribution of the gas reactant in the CVD reactor with a top-injection scheme: (a) Case 4; (b) Case 5; (c) Case 6.

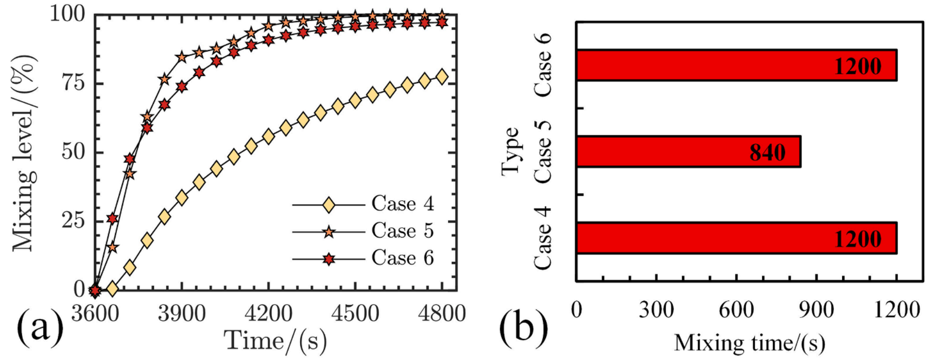

Fig. 11. Comparison of the mixing level and the mixing time between cases with a top-injection scheme: (a) the evolution of mixing level in the porous media zone; (b) the mixing time in the porous media zone.

indicate that Case 5 and Case 6 couldn't mix the gas reactant more quickly in the late stage of reaction when compared to Case 2 and Case 3, respectively. The present results show that a top-injector scheme could moderately enhance the mixing performance in the situation of Case 2, Case3, and hence improve the growth uniformity of the film.

4. Conclusions

In this work, a new CFD model was developed to simulate a special industrial-scale CVD reactor that needs to process thousands of substrate surfaces simultaneously. The model took advantage of the porous media based method, i.e., an effective way to avoid simulating substrate surfaces explicitly. The introduced method is also capable of simulating energy exchange between two phases in the porous media zone. The simulation results on temperature evolution in the reactor can match the experimental data well.

Based on this model, a series of numerical experiments have been carried out to investigate the mixing performance in the CVD reactor under different design schemes. It was found that the mass transport mechanism in the base case was diffusion dominated and thus the mixing performance was poor. Rearranging substrate distribution and introducing heat loss from the reactor wall were found to be effective approaches that can enhance natural convection. Furthermore, a top-injection scheme performed moderately better than a side-injection scheme. The modeling method presented here should be applicable to similar industrial reactors, which are used to produce a large amount of products in a single batch.

Declaration of Competing Interest

The authors declare that they have no known competing financial interests or personal relationships that could have appeared to influence the work reported in this paper.

Acknowledgements

We are grateful for the financial support from the National Natural Science Foundation of China (21978184), the Natural Science Foundation of Jiangsu Province (BK20170062), the National Key Research and Development Program of China (International S&T Cooperation Program, ISTCP, 2016YFE0101200), the “Jiangsu Innovation and Entrepreneurship (Shuang Chuang) Program”, the “Jiangsu Specially-Appointed Professors Program”, and the “Priority Academic Program Development (PAPD) of Jiangsu Higher Education Institutions”. The authors also thank Zhenkai Liao and Chao Shang, who provide substantial assistance in experiments.

References

[1] C.R. Kleijn, R. Dorsman, K.J. Kuijlaars, M. Okkerse, H. van Santen, Multi-scale modeling of chemical vapor deposition processes for thin film technology, J. Cryst. Growth 303 (2007) 362–380.
[2] A.C. Jones, M.L. Hitchman, Chemical Vapour Deposition: Precursors, Processes and Applications, Royal society of chemistry, Cambridge, 2009.
[3] Y. Xu, X.-T. Yan, Chemical Vapour Deposition: An Integrated Engineering Design for Advanced Materials, Springer, London, 2010.
[4] M. Lubej, I. Plazl, Theoretical and experimental study of iron catalyst preparation by chemical vapor deposition of ferrocene in air, Chem. Eng. J. 242 (2014) 306–312.
[5] Y.-C. Chuang, C.-T. Chen, Mathematical modeling and optimal design of an MOCVD reactor for GaAs film growth, J. Taiwan Inst. Chem. Eng. 45 (2014) 254–267.
[6] X.G. Li, W.D. Xiao, Model on transport phenomena and control of rod growth uniformity in siemens CVD reactor, Comput. Chem. Eng. 117 (2018) 351–358.
[7] Z. Nie, J. Deng, Y. Zhou, S. Wen, Y. Hou, Prediction of thermal and electrical behavior of silicon rod for a 48-rod Siemens reactor by direct current power, Int. Commun. Heat Mass Transfer 88 (2017) 148–159.
[8] X.G. Li, W.D. Xiao, Silane pyrolysis to silicon rod in a bell-jar reactor at high temperature and pressure: modeling and simulation, Ind. Eng. Chem. Res. 55 (2016) 4887–4896.
[9] Z. Huang, S. Qie, X. Quan, K. Guo, C. Liu, Numerical simulation of multiple polysilicon CVD reactors connected in series using CFD method, Can. J. Chem. Eng. 93 (2015) 1721–1729.
[10] P.A. Gkinis, I.G. Aviziotis, E.D. Koronaki, G.P. Gakis, A.G. Boudouvis, The effects of flow multiplicity on GaN deposition in a rotating disk CVD reactor, J. Cryst. Growth 458 (2017) 140–148.
[11] J. Li, J. Wang, J.-D. Cai, Y.-F. Xu, B.-F. Fan, G. Wang, Numerical simulation and analysis of process parameters of GaN-MOCVD reactor, Int. Commun. Heat Mass Transfer 91 (2018) 64–76.
[12] J. Li, Z.-Y. Fei, Y.-F. Xu, J. Wang, B.-F. Fan, X.-J. Ma, G. Wang, Study on the optimization of the deposition rate of planetary GaN-MOCVD films based on CFD simulation and the corresponding surface model, R. Soc. Open Sci. 5 (2018).
[13] Z. Zhang, H. Fang, Q. Yao, H. Yan, Z. Gan, Species transport and chemical reaction in a MOCVD reactor and their influence on the GaN growth uniformity, J. Cryst. Growth 454 (2016) 87–95.
[14] Z. Zhang, H. Fang, H. Yan, Z. Jiang, J. Zheng, Z. Gan, Influencing factors of GaN growth uniformity through orthogonal test analysis, Appl. Therm. Eng. 91 (2015) 53–61.
[15] G.P. Gakis, E.D. Koronaki, A.G. Boudouvis, Numerical investigation of multiple stationary and time-periodic flow regimes in vertical rotating disc CVD reactors, J. Cryst. Growth 432 (2015) 152–159.
[16] J. Cho, T.J. Mountziaris, Onset of flow recirculation in vertical rotating-disc chemical vapor deposition reactors, AIChE J. 59 (2013) 3530–3538.
[17] N. Cheimarios, M. Kavousanakis, G. Kokkoris, A.G. Boudouvis, Beware of symmetry breaking and periodic flow regimes in axisymmetric CVD reactor setups, Comput. Chem. Eng. 124 (2019) 124–132.
[18] J. Skibinski, P. Caban, T. Wejrzanowski, G.J. Oliver, K.J. Kurzydlowski, Numerical design of metal-organic vapour phase epitaxy process for gallium nitride epitaxial growth, Cryst. Res. Technol. 51 (2016) 762–770.
[19] C.H. Lin, W.T. Cheng, J.H. Lee, Effect of embedding a porous medium on the deposition rate in a vertical rotating MOCVD reactor based on CFD modeling, Int. Commun. Heat Mass Transfer 36 (2009) 680–685.
[20] C.C. Liao, S.S. Hsiau, T.C. Chuang, Modeling and designing a new gas injection diffusion system for metalorganic chemical vapor deposition, Heat Mass Transf. 54 (2018) 115–123.
[21] H. Ni, S. Lu, C. Chen, Modeling and simulation of silicon epitaxial growth in Siemens CVD reactor, J. Cryst. Growth 404 (2014) 89–99.
[22] H. Fang, Z. Zhang, Y. Pan, R. Ma, S. Liu, M. Wang, Systematic study of epitaxy growth uniformity in a specific MOCVD reactor, Cryst. Res. Technol. 49 (2014) 907–918.
[23] B. Mitrovic, A. Gurary, L. Kadinski, On the flow stability in vertical rotating disc MOCVD reactors under a wide range of process parameters, J. Cryst. Growth 287 (2006) 656–663.
[24] B. Mitrovic, A. Gurary, W. Quinn, Process conditions optimization for the maximum deposition rate and uniformity in vertical rotating disc MOCVD reactors based on CFD modeling, J. Cryst. Growth 303 (2007) 323–329.
[25] C.-F. Tseng, T.-Y. Tsai, Y.-H. Huang, M.-T. Lee, R.-H. Horng, Transport phenomena and the effects of reactor geometry for epitaxial GaN growth in a vertical MOCVD reactor, J. Cryst. Growth 432 (2015) 54–63.
[26] S. Makino, M. Inagaki, K. Nakashima, T. Kozawa, N. Horinouchi, A simplified reaction model and numerical analysis for Si deposition from the SiHCl3-H2 system in vertical rotating disk reactors, J. Cryst. Growth 454 (2016) 156–163.
[27] M. Li, J.F. Sopko, J.W. McCamy, Computational fluid dynamic modeling of tin oxide deposition in an impinging chemical vapor deposition reactor, Thin Solid Films 515 (2006) 1400–1410.
[28] Z. Nie, Y. Hou, J. Deng, P.A. Ramachandran, S. Wen, W. Ma, The combined effect of heat transfer and skin effect on Joule heating for silicon rod in Siemens reactor, Appl. Therm. Eng. 125 (2017) 856–869.
[29] Z. Nie, Y. Zhou, J. Deng, S. Wen, Y. Hou, Thermal and electrical behavior of silicon rod with varying radius in a 24-rod Siemens reactor considering skin effect and wall emissivity, Int. J. Heat Mass Transf. 111 (2017) 1142–1156.
[30] Z. Nie, P.A. Ramachandran, Y. Hou, Optimization of effective parameters on Siemens reactor to achieve potential maximum deposition radius: An energy consumption analysis and numerical simulation, Int. J. Heat Mass Transf. 117 (2018) 1083–1098.
[31] F.R.S.G.K. Batchelor, An Introduction to Fluid Dynamics, 1 ed., Cambridge University Press, Cambridge, 2000.
[32] B.E. Poling, J.M. Prausnitz, O.C. John Paul, R.C. Reid, The Properties of Gases and Liquids, 5 ed.,, McGraw-Hill, New York, 2001.
[33] R.B. Bird, W.E. Stewart, E.N. Lightfoot, D.J. Klingenberg, Introductory Transport Phenomena, Wiley Global Education, 2015.
[34] D.A. Nield, A. Bejan, Convection in Porous Media, 5 ed., Springer, Berlin, 2017.
[35] K. Vafai, Handbook of Porous Media, 3 ed., CRC Press, Boca Raton, 2015.
[36] J. Xiao, J. Han, F. Zhang, X.D. Chen, Numerical simulation of crystallization fouling: taking into account fouling layer structures, Heat Transfer Eng. 38 (2017) 775–785.
[37] D. Kim, S.J. Kim, A. Ortega, Compact modeling of fluid flow and heat transfer in pin fin heat sinks, J. Electron. Packag. 126 (2004) 342–350.
[38] T.-M. Jeng, S.-C. Tzeng, A semi-empirical model for estimating permeability and inertial coefficient of pin-fin heat sinks, Int. J. Heat Mass Transf. 48 (2005) 3140–3150.
[39] R.H. Perry, D.W. Green, Perry’s Chemical Engineer’s Handbook, 8 ed., McGraw-Hill, New York, 2007.
[40] W. Schotte, Prediction of the molar volume at the normal boiling point, Chem. Eng. J. 48 (1992) 167–172.
[41] E.L. Cussler, Diffusion: mass transfer in fluid systems, Cambridge university press2009.
[42] R. Millington, J. Quirk, Permeability of porous solids, Trans. Faraday Soc. 57 (1961) 1200–1207.
[43] A. Burcat, Thermochemical Data for Combustion Calculations, Springer, New York, Combustion chemistry, 1984, pp. 455–473.
[44] COMSOL Multiphysics® v. 5.4 www.comsol.com, COMSOL AB, Stockholm, Sweden, 2019.
[45] C. Li, J. Xiao, Y. Zhang, X.D. Chen, Mixing in a soft-elastic reactor (SER): a simulation study, Can. J. Chem. Eng. 97 (2019) 676–686.
[46] J. Xiao, C. Zou, M. Liu, G. Zhang, G. Delaplace, R. Jeantet, X.D. Chen, Mixing in a soft-elastic reactor (SER) characterized using an RGB based image analysis method, Chem. Eng. Sci. 181 (2018) 272–285.